Mechanically amplified milli-Newton thrust balance for helicon plasma thrusters

IEPC-2019-595

Presented at the 36th International Electric Propulsion Conference
University of Vienna, Austria
September 15-20, 2019

ir. M. Wijnen* and dr. J. Navarro-Cavallé† and dr. P. Fajardo‡ and prof.dr. E. Ahedo§
Universidad Carlos III de Madrid, Leganés, Madrid, 28911, Spain

Direct thrust measurements by means of a thrust balance are the golden standard for measuring thrust and concurrently the specific impulse in electric thrusters. To measure the thrust of a medium power (300-1000W) Helicon Plasma Thruster (HPT) we propose a thrust balance design based on the VAHPER concept. The thrust balance is designed to measure thrust between 1-100 mN for thrusters weighing up to 50 kg.

The thrust balance has a angular magnification of 31x and is shown to behave like a damped harmonic oscillator with a torsional stiffness of 48.2 N-rad/m, moment of inertia of 12.2 kg-m^2 and a natural frequency of 316 mHz. A variable damping system is able to provide up to critical damping with an optimal damping ratio of 0.78 corresponding to a settling time of only 1.8 s.

Preliminary calibration shows a compliance of 160 μm/mN corresponding to about 100 μm/mN when loaded with a 5 kg thruster. Noise levels are of the order of 2-5 μm.

To accommodate the particularities of a medium-power RF thruster the thrust balance design includes the following features: an optical displacement sensor, water cooling, liquid electrical connectors, on-board, in-vacuum electronics that account for auto-leveling, in-situ calibration and temperature measurements.

Furthermore, a contact-less power transfer mechanism is proposed, based on resonant inductive coupling operating at 13.56 MHz to mechanically decouple the RF power supply line., promising high power efficiency ($> 95\%$) with a large bandwidth (1 MHz).

*PhD Student, dept. ing. Aeroespacial, mwijnen@pa.uc3m.es.
†Assistant Professor dept. ing. Aeroespacial, jnavarr@ing.uc3m.es.
‡Associate Professor, dept. ing. Aeroespacial, pfajardo@ing.uc3m.es.
§Professor, dept. ing. Aeroespacial, eahedo@ing.uc3m.es.

Nomenclature

α_0 = correction factor
β = torsional viscous damping
γ, θ = angles
ζ = damping ratio
κ = torsional spring constant
σ = conductivity
τ = torque
ω = angluar velocity

b = viscous damping
$\mathbf{B}$ = magnetic field
C = capacitance
d = displacement
E = Young's modulus
E_k = kinetic energy
$\mathbf{E}$ = electric field
F = force
$\mathbf{g}$ = gravity
I = moment of inertia, second area of moment, current
$\mathbf{J}$ = current density
m = mass
M = mass, mutual inductance
L = length, inductance
$\mathcal{L}$ = Lagrange function
q = generalized variables
Q = generalized forces
$\mathbf{r}$ = position vector
R = resistance
S = pole projection area
T = thrust
U = potential energy
V = voltage
w = deflection
Z = impedance

I. Introduction

Helicon plasma thrusters are a type of electrode-less thruster that uses helicon waves to reach high ionization degrees. These waves are excited by (half-)helical antennas at frequencies in the Megahertz range. These thrusters rely furthermore on magnetic nozzles for plasma acceleration by converting the thermal electron energy into ion kinetic energy. Trust is generated by the magnet repulsion between diamagnetic electron currents and the (electro-)magnets of the thruster.

These thrusters have been investigated by the electric propulsion group (EP2) of Universidad Carlos III de Madrid (UC3M) for several years, both theoretically[?,1–4] and experimentally.[5,6] The current iteration HPT05M of the prototype developed jointly with SENER sistemas y ingienera, operates with 300-600W of RF power at 13.56 MHz, magnetics fields between 0.1-0.2 T and mass flow rates of xenon and argon of 5-50 sccm. All current experimental work has been performed mainly with electrostatic probes. Current performance estimates are 5-8 mN of thrust, 750-1200s of specific impulse and 7-10% of efficiency.[6] However electrostatic probes only provide indirect measurements. The golden standard are still direct thrust measurements by means of a thrust stand. This has driven the development of a new thrust balance designed to accommodate the HPT05M prototype.

The HPT05M, which at 5 kg has an estimated thrust-to-weight ratio of only 2 mN/kg, produces strong RF fields, requires electrical currents of up to 30 A, and presents thermal heat loads of up 2 kW. This imposes a set of stringent requirements on the design. The thrust balance design was based of the VAHPER design from NASA's Marshall Space Flight centre[7] which has a mechanical amplification mechanism to increase the resolution. In this paper we present a dynamic analysis based on the Lagrange formalism to analyse the balance performance. We also will detail several strategies for meeting the challenges posed by the HPT05M, such as liquid metal connectors, water cooling and wireless power transfer. We also analyzed and measured the damping system and provide a first, preliminary calibration. A CAD drawing of the design (as it it is currently built) is shown in figure 1, with the most important feature labeled.

II. Mechanics

A. Kinematics

We first start with the kinematics of the setup. This analysis is based on that from[7] and the reader is referred to that paper for the derivation of the equations presented here. As can be seen in figure 2 we define the reference frame centered at O with the x-axis rightwards, and the y-axis upwards.

The mechanism consists of three members numbered $1, 2, 3$. The first member is an L-shape suspended at its corner from the reference frame at O. It is suspended by means of a torsional flexure with torsional spring constant κ_O. The second member is also suspended from the reference frame at A by a torsional spring (constant κ_A). The primary and secondary member are then interconnected with a third element (3) joined at B and C by torsional springs (with κ_B, κ_c respectively). The thruster, with mass M, is suspended from the bottom of element 1, while a counterweight with mass m is suspended on the right end of element 2.

The centers of mass (CoM) of all elements i are noted cm_i, where we numbered the thruster and the counterweight as 4 and 5, respectively. The point of element 2 where the displacement is measured is labeled E. Point D is the point where the damping force acts. Whereas point O and A are fixed to the reference frame, points B, C, D and E can move; when not in their initial position (element 2 horizontal) they are denoted with a prime i.e. B', C', D', E'. Then there are four relevant angles, $\theta_1 - \theta_4$ as show in figure 2. Lastly it has to be noted that the gravity vector is pointing in the $-y$ direction.

The quantity of interest in conventional pendulum balances is the horizontal displacement of cm_4 - here denoted d_2 - and how it is related to the applied force T. However in this particular arrangement the vertical

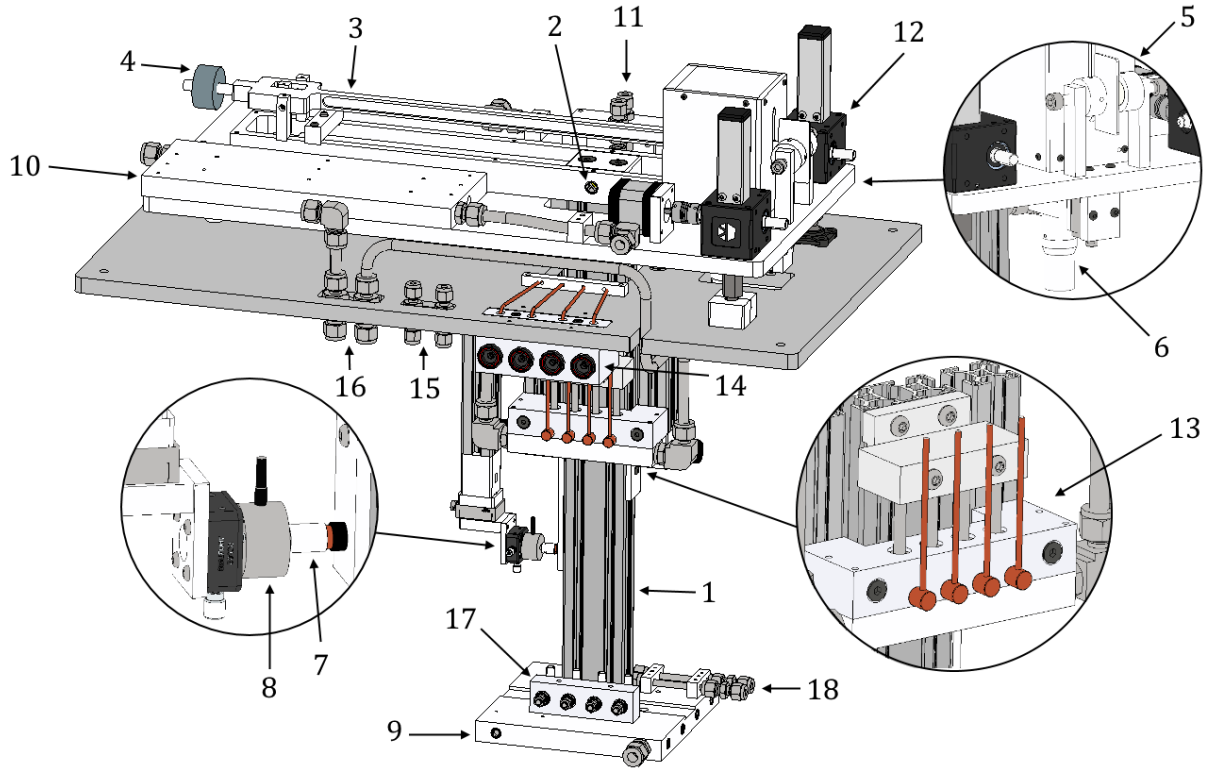

Figure 1. CAD drawing of the thrust balance design. 1) Primary arm. 2) Pivot O 3) Secondary arm. 4) Counterweight. 5) Eddy current damper. 6) Displacement sensor. 7) Voice coil. 8) Load cell. 9) Water cooled mounting plate. 10) Water cooled electronics plate. 11) Propellant line mounting point. 12) Motorized screw jack for auto-leveling. 13) Liquid metal connectors. 14) Power supply user interface (UI). 15) Propellant line UI. 16) Cooling water UI. 17) Power supply thruster interface. 18) Propellant supply thruster interface.

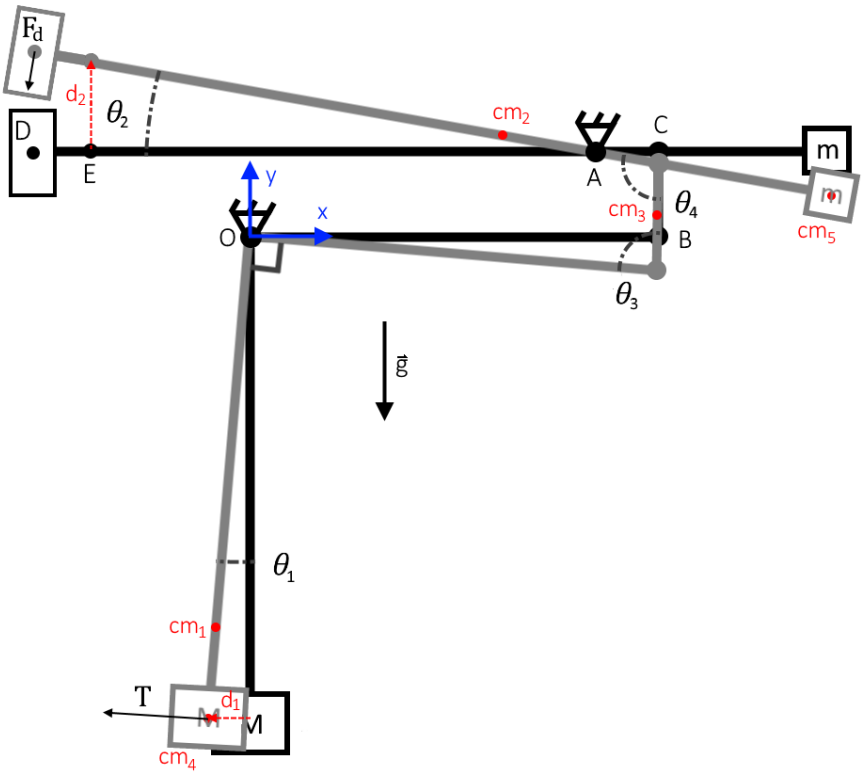

Figure 2. Schematic of the thrust balance mechanism.

displacement of D, denoted d_2 can be shown to be related to d_1 as follows.

$$d_2 = 2L_{AE} \sin\left(\frac{\theta_2}{2}\right) \tag{1}$$

$$\theta_2 = \theta_1 + \theta_3 + \theta_4 - \pi \tag{2}$$

$$\theta_1 = 2\sin^{-1}\left(\frac{d_1}{L_4}\right) \tag{3}$$

$$\theta_3 = \cos^{-1}\left(\frac{L_{AB}^2 + L_{AB'}^2 - L_{OA}^2}{2L_{OA}L_{AB'}}\right) + \cos^{-1}\left(\frac{L_{AB'}^2 + L_{BC}^2 - L_{AC}^2}{2L_{AB'}L_{BC}}\right) \tag{4}$$

$$\theta_4 = \cos^{-1}\left(\frac{L_{AC}^2 + L_{BC}^2 - L_{AB'}^2}{2L_{AC}L_{BC}}\right) \tag{5}$$

$$L_{AB'}^2 = L_{OB}^2 + L_{OA}^2 - 2L_{OB}L_{OA}\cos\left(\gamma + \theta_1\right) \tag{6}$$

$$\gamma = \cos^{-1}\left(\frac{L_{OA}^2 + L_{OB}^2 - L_{AB}^2}{2L_{OA}L_{OB}}\right) \tag{7}$$

where $\gamma \equiv \angle AOB$. The variables L_i denote the length from the centre of mass cm_i to its corresponding point of rotation while L_{jk} is the length between the points j, k.

Note that here, it is implicit that θ_3, θ_4 are initially right angles. It can be seen that d_2 is a function of θ_2 which is in turn a function of θ_1, which is a function of d_1. All of the other parameters are constant. Therefore there is a functional relationship $d_2 = f(d_1)$. This relationship can be calculated by solving the above equations for a range of d_1. This relationship is linear; for the dimensions shown in table 1 it follows that $d_2 = 19.62 \cdot d_1$, so the magnification is almost 20 times. However this is assuming that the displacement would be measured at a distance L_{OM}. However this is not practical nor desirable. Therefore it makes more sense to speak of the ratio between θ_2 and θ_2 which is amplified by a factor 31.

The magnification is dependent on the inter-pivot distance L_{AC} which is a design parameter. The smaller this distance the larger the magnification. For larger distances gravity dominates the thrust balance response,

Table 1. Dimensions of the schematic thrust balance.

Point	x [m]	y [m]	κ [N-m/rad]
O	0.000	0.000	0.19160
A	0.300	0.045	0.02330
B	0.310	0.000	0.01165
C	0.310	0.045	0.01165
D	-0.175	0.045	-
E	-0.105	0.045	-
M	0.000	0.640	-

while for smaller distances the springs dominate. The displacement d_2 as a function of the distance L_{AC} for a 5 kg thruster and 10 mN of thrust (representative of the HPT05M[5]) is shown in figure 3 and clearly displays this behaviour. For heavier thrusters this peak shifts leftward, while higher thrust shifts the whole curve upward. The maximum displacement d_2 for this case is found at an inter-pivot distance of 10.4 mm. For this reason the design value was set at $L_{AC} = 10$ mm.

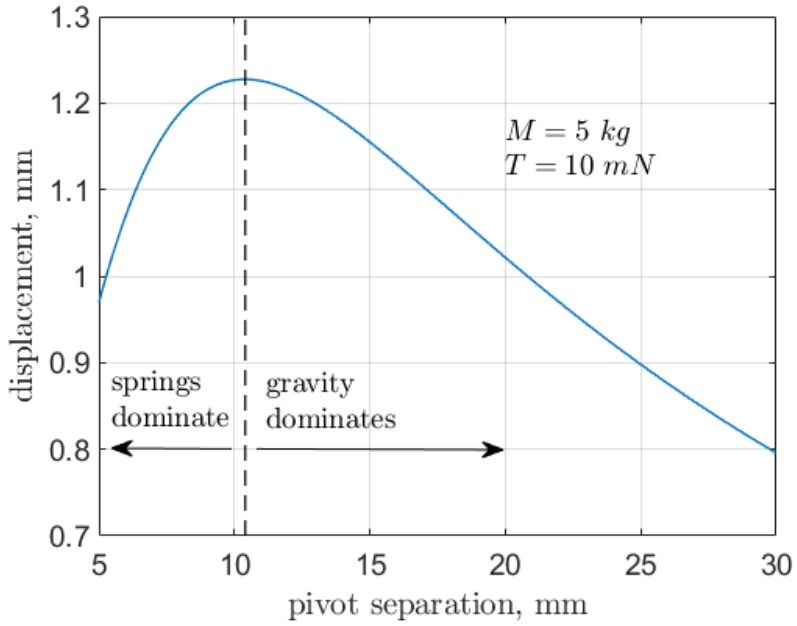

Figure 3. Displacement d_2 as a function of varying inter-pivot distance L_{AC} for a 5 kg thruster, producing 10 mN of thrust.

The compliance of the thrust balance can be obtained from a force balance at all four pivots (0, A, B, and C in Fig. 1). The resulting relationship between the applied thrust T and the angle θ_1 is given by:

$$T = \frac{\tau_O + \tau_{B'}}{L_{OM}} + Mg\sin(\theta_1) + \frac{(\tau_A + \tau_{C'})\, L_{OB}\cos\left(\frac{\pi}{2} - \theta_3\right)}{L_{OM} L_{AC}\cos\left(\frac{\pi}{2} - \theta_3\right)} \tag{8}$$

where,

$$\tau_O = \kappa_O \theta_1 \qquad \tau_{B'} = \kappa_B\left(\theta_3 - \frac{\pi}{2}\right) \tag{9}$$

$$\tau_A = \kappa_A \theta_2 \qquad \tau_{C'} = \kappa_C\left(\theta_4 - \frac{\pi}{2}\right) \tag{10}$$

Combining (1) and (8) the full kinematics response of the thrust balance can be calculated. For the dimensions in table 1 we have plotted in figure 4 the minimum and maximum measurable thrust as a function of

the thruster mass assuming a sensor range of 12 mm and a resolution of 1 μm. The compliance (inverse of the stiffness) of the balance also changes with thruster mass and varies from about 0.2 m/N for a 1 kg thruster to about 0.012 m/N for a 100 kg thruster as can be seen in figure 5. For a 5 kg thruster like the HPT05M a compliance of about 0.12 m/N is expected.

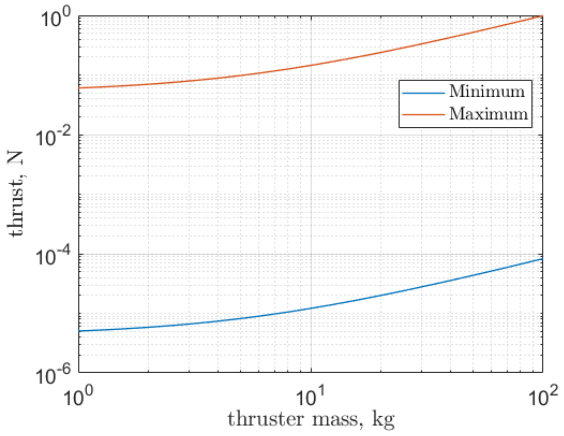

Figure 4. Measurable thrust range for different thruster mass, for a resolution of 1 μm and a range of 12 mm.

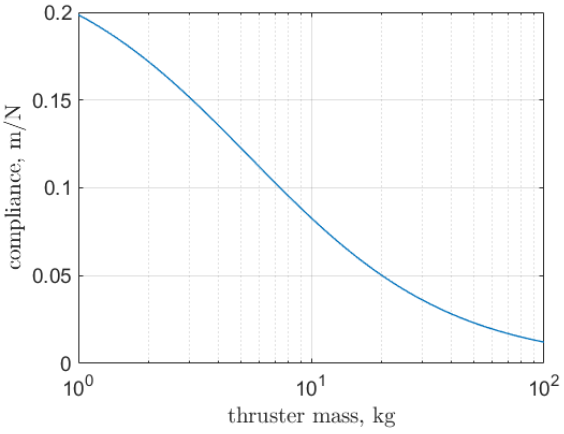

Figure 5. Compliance of the thrust balance as a function of thruster mass.

B. Dynamics

The aforementioned section only addressed the kinematics of the balance. However the dynamic behaviour is also of interest as it informs us about the time-response of the system. Although at first the system does not look like a simple harmonic oscillator it can be shown to behave like one.

The system can be analyzed using Lagrangian mechanics. We consider the system formed by 6 elements and start with defining the Lagrange function:

$$\mathcal{L} = E_k - U \tag{11}$$

with E_k the kinetic energy and U the potential energy which are defined as:

$$E_k = \frac{1}{2}\sum_i m_i \dot{r}_i^2 + \omega_i^T \bar{\bar{I}}_i \omega_i \tag{12}$$

$$U = \sum_i \frac{1}{2}\kappa_i \theta_i^2 + m_i \vec{g} \cdot \mathbf{r}_i \tag{13}$$

here $\mathbf{r}_i$ are the position vectors of the centers of mass of the 5 elements, and $\dot{\mathbf{r}}_i$ their time derivatives, m_i are the corresponding masses. The ω_i are the angular velocities of the rigid members, only defined for $i = 1, 2$ and $\bar{\bar{I}}_i$ are the corresponding inertia matrix. Lastly κ_i are the torsional spring constants of the four pivots and $\vec{g} = -g\,\hat{\mathbf{y}}$ is the gravitational acceleration.

It is important to note that all quantities in the above expressions are a only a function of the angle θ_1 and it's time derivative. This angle θ, dropping the subscript for clarity, is the single generalized coordinate that determines this system. Although the other angles are non-linear functions of θ, since $\theta \ll 1°$, and we are interested in motion around the point $\theta = 0$, these functions can be linearized.

For the analysis we consider the Euler-Lagrange equation, which reads:

$$\frac{d}{dt}\left(\frac{d\mathcal{L}}{d\dot{q}_j}\right) - \frac{d\mathcal{L}}{dq_j} = Q_j \tag{14}$$

where q_j are the generalized variables and Q_j are the generalized forces:

$$Q_j = \sum_i \mathbf{F}_i \cdot \frac{\partial \mathbf{r}_i}{\partial q_j} = \sum_i \mathbf{F}_i \cdot \frac{\partial \dot{\mathbf{r}}_i}{\partial \dot{q}_j} \tag{15}$$

where the second equality is called the velocity formulation. For now, we consider $Q_j = 0$ and $q_j = \theta$ resulting in:

$$\frac{d}{dt}\left(\frac{d\mathcal{L}}{d\dot{\theta}}\right) - \frac{d\mathcal{L}}{d\theta} = 0 \tag{16}$$

Solving this equation will yield the equation of motion for the system. To solve this equation all $\mathbf{r}_i, \dot{\mathbf{r}}_i$ and ω_i need to be known and are, for this purpose, tabulated in table 2. L_i are the lengths from the center of mass of element i to A, or to O for $i = 1, 4$. As mentioned before the angles θ_i are (nonlinear) functions of θ. In linearized form they can be written as follows:

$$\theta_1 = \theta \tag{17}$$

$$\theta_2 = n\theta \quad \text{with} \quad n = 1 + \theta_3'(0) + \theta_4'(0) \tag{18}$$

$$\theta_3 = \frac{\pi}{2} + \theta_3'(0)\theta \tag{19}$$

$$\theta_4 = \frac{\pi}{2} + \theta_4'(0)\theta \tag{20}$$

note that, in the previous equations, the prime denotes $d/d\theta$. We now write out the terms of the Euler-

Table 2. Position, velocity and angular velocity vectors for elements i.

i	$\mathbf{r}_i$	$\dot{\mathbf{r}}_i$	ω_i
1	$\begin{bmatrix} \cos\theta & \sin\theta \\ -\sin\theta & \cos\theta \end{bmatrix} \begin{bmatrix} x_{1,0} \\ y_{1,0} \end{bmatrix}$	$-\begin{bmatrix} \sin\theta - \cos\theta \\ \cos\theta \quad \sin\theta \end{bmatrix} \begin{bmatrix} x_{1,0} \\ y_{1,0} \end{bmatrix} \dot{\theta}$	$-\dot{\theta}$
2	$\mathbf{r}_A - L_2(\cos n\theta\, \hat{\mathbf{x}} - \sin n\theta\, \hat{\mathbf{y}})$	$L_2(\sin n\theta\, \hat{\mathbf{x}} + \cos n\theta\, \hat{\mathbf{y}})n\dot{\theta}$	$-n\dot{\theta}$
3	N/A	N/A	
4	$-L_4(\sin\theta\, \hat{\mathbf{x}} + \cos\theta\, \hat{\mathbf{y}})$	$-L_4(\cos\theta\, \hat{\mathbf{x}} - \sin\theta\, \hat{\mathbf{y}})\dot{\theta}$	N/A
5	$\mathbf{r}_A + L_5(\cos n\theta\, \hat{\mathbf{x}} - \sin n\theta\, \hat{\mathbf{y}})$	$-L_5(\sin n\theta\, \hat{\mathbf{x}} + \cos n\theta\, \hat{\mathbf{y}})n\dot{\theta}$	N/A

Lagrange equation for $i = 1..5$

$$\sum_{i=1}^{N} \frac{1}{2} m_i \dot{r}_i^2 = \frac{1}{2}(m_1 L_1^2 + m_2 n^2 L_2^2 + m_4 L_4^2 + m_5 n^2 L_5^2)\dot{\theta}^2 \tag{21}$$

$$\sum_{i=1}^{N} \frac{1}{2} I_i \omega_i^2 = \frac{1}{2}(I_1 + n^2 I_2)\dot{\theta}^2 \tag{22}$$

$$\begin{aligned} -\sum_{i=1}^{N} m_i \mathbf{g} \cdot \mathbf{r}_i = g[&m_1(y_{1,0}\cos\theta - x_{1,0}\sin\theta) + m_2(y_A + L_2 \sin n\theta) \\ &- m_4 L_4 \cos\theta + m_5(y_A - L_5 \sin n\theta)] \end{aligned} \tag{23}$$

$$\sum_{i=1}^{N} \frac{1}{2} \kappa_i \theta_i^2 = \frac{1}{2}(\kappa_1 + n^2\kappa_2 + [\theta_3'(0)]^2\kappa_3 + [\theta_4'(0)]^2\kappa_4)\theta^2 \tag{24}$$

note that in the term $\frac{1}{2}\kappa_i\theta_i^2$ for $i = 3, 4$ it should actually be $(\theta_i - \frac{\pi}{2})^2$, however due to linearization, the constant factor of $\frac{\pi}{2}$ cancels out and we are left with the theta primes evaluated at zero.

From the above equations it is evident that the kinetic energy part is only dependent on $\dot{\theta}$ and the potential part is only dependent on θ. The Euler-Lagrange equation for this system can now be written as:

$$\begin{aligned} &(m_1 L_1^2 + m_2 n^2 L_2^2 + m_4 L_4^2 + m_5 n^2 L_5^2 + I_1 + n^2 I_2)\ddot{\theta} \\ &+ (\kappa_1 + n^2\kappa_2 + [\theta_3'(0)]^2\kappa_3 + [\theta_4'(0)]^2\kappa_4 - g m_1 y_{1,0} + g m_4 L_4)\theta \\ &= g(m_1 x_{1,0} + n m_5 L_5 - n m_2 L_2) \end{aligned} \tag{25}$$

Note that the approximations $\sin\theta \simeq \theta$ and $\cos\theta \simeq 1$ are used in the in the gravitational term. It is interesting to see that the spring force of the flexures at A and C is multiplied by a factor n^2 (which is equal

to $[\theta_4'(0)]^2$ and of the order of 10^3 as we will see later). The above expression represents a harmonic oscillator with an effective moment of inertia I, an effective torsional spring constant κ and a constant offset τ_0:

$$I\ddot{\theta} + \kappa\theta = \tau_0 \tag{26}$$

The constant term is the sum of the torques $\tau_0 = gm_1x_{1,0} + gnm_5L_5 - gnm_2L_2$. The distance of the counterweight to the pivot A, L_5, is variable and can be used to balance out the system, by choosing L_5 such that $\tau_0 = 0$. The natural frequency of the system is given by $\omega_0 = \sqrt{\kappa/I}$.

As shown in figure 2 there are two forces applied to the system, T the thrust operating at cm_4 and F_d the damping force, which is proportional to the angular velocity $\dot{\theta}_2$ operating at point D. To include these forces we now consider Q_j non-zero:

$$Q_4 = \mathbf{F} \cdot \frac{\partial \mathbf{r}_4}{\partial \theta} = TL_4 \tag{27}$$

$$Q_D = \mathbf{F} \cdot \frac{\partial \mathbf{r}_D}{\partial \theta} = -bn^2L_D^2\dot{\theta} \tag{28}$$

where $\mathbf{r}_D = \mathbf{r}_A - L_D(\cos n\theta\,\hat{\mathbf{x}} - \sin n\theta\,\hat{\mathbf{y}})$. The new equation of motion then becomes:

$$I\ddot{\theta} + \beta\dot{\theta} + \kappa\theta = \tau(t) + \tau_0 \tag{29}$$

with $\beta = bn^2L_D^2$ being the torsional viscous damping factor, and $\tau = TL_4$ the torque due to the thrust. It is perfectly clear that the balance behaves as a damped harmonic oscillator in first approximation.

For the dimensions in table 1 the linearization yields the following values: $\theta_3'(0) = -1$ which means that $n = \theta_4'(0)$ which is equal to 31.68, very similar to the factor 31 we found in the kinematic analysis, within an error of 2%.

We can obtain the moments of inertia and the masses of all elements from our CAD model and use these to estimate the natural frequency of the system as well as the viscous damping coefficient needed to provide sufficient damping. The values are reported in table 3. Using equations (25) and (26) we can calculate the effective moment of inertia $I = 14.2$ kg-m^2, and the effective force constant $\kappa = 79.5$ N-m/rad. Combined this yields a natural frequency of 0.376 Hz equivalent to a period of about 2.66 seconds.

Table 3. Mass and moment of inertia of all elements i

i	m_i [kg]	L_i [mm]	I_i [kg-m^2]
1	3.710	373.0	$150.92 \cdot 10^{-3}$
2	0.236	116.9	$6.86 \cdot 10^{-3}$
3	0.000	-	-
4	5.000	640.0	-
5	0.271	97.4	-

III. Damping

To have a response that is close to the step response of the applied thrust and to prevent the system oscillating, a damping force is required. The equation of motion for the damped harmonic oscillator can be rewritten as:

$$\ddot{\theta} + 2\zeta\omega_0\dot{\theta} + \omega_0^2\theta = \frac{\tau}{I} \qquad \zeta = \frac{\beta}{2\sqrt{\kappa I}} \qquad \omega_0 = \sqrt{\frac{\kappa}{I}} \tag{30}$$

Generally damping ratios of $0.4 < \zeta < 0.8$ give a good step response.[8] With $\beta = bn^2L_D^2$ we can estimate the value of the viscious damping coefficient. The ratio of ζ to b, for κ, I as mentioned above, $L = 485$ mm and $n = 31$ is 3.4. This results in a required viscous damping coefficient of $0.12 < b < 0.24$ kg/s.

The damping can be achieved by means of Eddy current damping, which is contact-less and well suited for vacuum. When a conductor moves through a magnetic field, Eddy currents are induced inside the conductor.

These charges moving in the magnetic field then experience a Lorentz force which is proportional to and in opposite direction of the velocity. The induced current density and the resulting force are:

$$\mathbf{J} = \sigma\left(\mathbf{E} + \mathbf{v} \times \mathbf{B}\right) \qquad \mathbf{F}_d = \int_V \mathbf{J} \times \mathbf{B} \mathrm{dV} \tag{31}$$

Suppose we have a thin metal plate (thickness δ) moving with velocity $\mathbf{v} = v\hat{x}$ in a homogeneous magnetic field $\mathbf{B} = B_z\hat{z}$ created by two square magnets with pole projection S. The induced currents will be in the $-y$ direction and will results in charge separation and therefore an electric field, also in the $-y$ direction and can be shown to be proportional to both the velocity and the magnetic field as well as some geometric factor. The volume integral (Eq. (31)) can be approximated with:[9]

$$F_d = -\sigma\delta S B_z^2 \alpha_0 v = -bv \tag{32}$$

where α_0 includes the geometric factor as well as a correction for a finite plate. For a finite conductor the Eddy currents perpendicular to the boundaries are zero. The real current distribution can be calculated using the method of image currents.[9] However to avoid this complexity and since in our setup we use cylindrical instead of square magnets the analysis was performed using Comsol. The conductive plate is made of aluminium ($\sigma = 3.77 \cdot 10^7$ S/m), is 30 mm x 60 mm and has thickness $\delta = 2$ mm. To estimate the magnetic field we can use equation (32) (with $\alpha_0 \sim 0.4$ according to Bae[9]) it follows that we need a field of about 1100-1600 G to cover the desired range of damping ratios.

After varying several parameters we settled on a damping system consisting of the above mentioned plate, and two 20 mm diameter x 5 mm height, cylindrical NdFeB magnets with a remanence of 1.3T, spaced a distance d apart. To be able to vary the magnetic field, d is variable by means of screws. Figure 6 shows a plot of the viscous damping coefficient as a function of the distance. The blue line is the viscous damping coefficient as simulated with Comsol and is plotted along the right axis. The red dots is the measured damping ratio plotted along the left axis. The measurements were performed without a thruster present (but with the cold-plate). The calculated stiffness and moment of inertia of this system are 12.2 kg-m^2 and 48.2 N-rad/m leading to a ratio between ζ and b of 4.66, which was used to scale both axes. Although both simulation and measurement follow the same trend $\propto \exp(-0.16d)$ their ratio is 1.8 rather than the calculated 4.7. The actual damping is a factor 2.6 lower than calculated. It's not yet clear what causes this. We measured the magnetic field and compared this with the magnetic field as calculated with Comsol and the results agree reasonably well. We have yet to find an explanation for this discrepancy. Regardless, in the current setup the desired range of damping is covered by the range of magnet separations; however, for very heavy thrusters it might not be.

It is interesting to note that when plotting the damping coefficient versus the square of the average magnetic field inside the pole projection the slope is about 9.65, which from (32) yields $\alpha_0 = 0.4$ as was estimated beforehand, showing that equation 32 is a good approximation.

The optimal damping is that for which the settling time is minimal. Using the parameters derived from our Lagrangian model we simulated the settling time for different values of the normalized damping coefficient ζ, resulting in plot 7. This particular plot was made with just the cooling plate and without the thruster. The optimal damping ratio is about $\zeta = 0.78$ with a settling of time 1.8s. We also inferred the settling time and damping ratio from the measured response of the system to a step input for various separation distances of the magnets which are the purple dots in figure 7. As is apparent the measurement and simulation agree well.

IV. Displacement Sensor

The quantity measured directly is the displacement of point D (in fig. 2). There are many different displacement sensors: inductive (LVDT), capacitive, interferometry, triangulation etc. For this particular balance we wanted a sensor that was impervious to EMI as the strong RF fields of a Helicon thruster are known to wreak havoc on electrical systems. Other drivers are a reasonable measurement range and a good resolution. For an expected compliance of about 0.1 m/N (fig. 5), a target thrust range of 100 mN and a resolution of 0.1 mN or better the sensor range and resolution need to be at least 10 mm and 10 μm respectively. In the end we've settled on a confocal chromatic sensor CSS-Prima from STIL.

Confocal chromatic sensors consist of a white light source, a system of lenses (the 'optical pen') and a spectrometer. The white light is refracted by the optical pen. As different wavelengths are focused at different

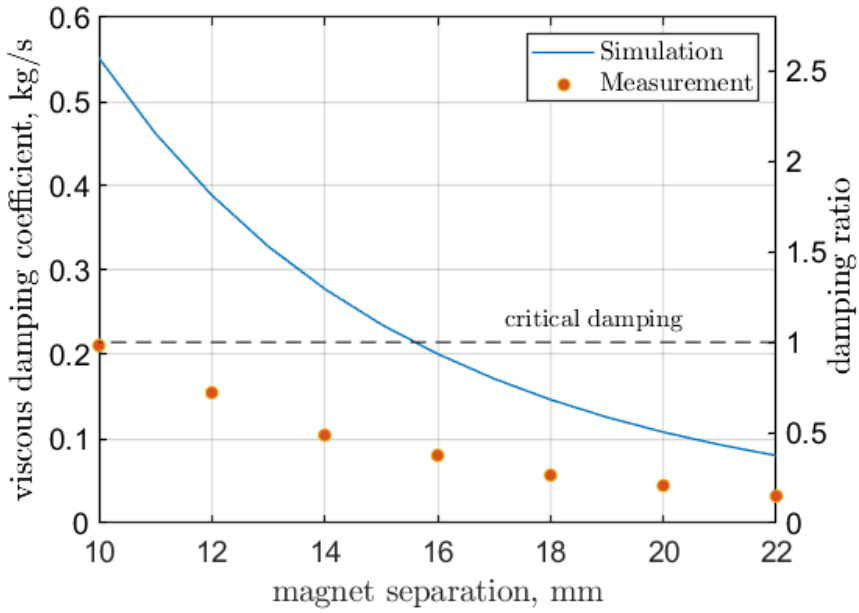

Figure 6. Damping coefficient as a function of the spacing between the magnets. The simulated data refers to the left axis, while the measurements refer to the right axis.

distances from the lenses the spectrum of the reflected light is related to the distance of the reflecting surface to the optical pen. Both the emitted and reflected light are coupled through a single optical fiber to and from the focal element. Using an optical feedthrough the in-vacuum path only consist of passive elements (fiber, optical pen) while the light source, spectrometer and other electronics all reside outside of vacuum chamber far away from the RF fields of the thruster. The range and resolution can be changed by changing the optical pen. For this particular application we are using the CL5-MG20 optical pen which has a measurement range of 12 mm and a resolution of 0.4 μm.

V. Calibration

Since the compliance of the thrust balance is dependent upon the the mass of the thruster, additional stiffness from gas, power and cooling lines as well as thermal drifts it is important that the thrust balance can be calibrated repeatedly, preferably in-situ without breaking the vacuum. Calibration is done by applying a known force while measuring the displacement, for a range of loads spanning the desired measurement range.

We've chosen a calibration system using a voice coil. Voice coils consist of a small solenoid that applies a force on a small magnet linearly proportional to the current applied. Although the force constant is constant in a small region and dependent on the relative position of the solenoid and the magnet. It is therefore not advisable to calculate the applied force from the applied current using the force constant provided by the manufacturer. Instead we mounted the magnet on a calibrated load cell and directly measured the applied force, circumventing the uncertainties in the voice coil force constant. Although the load cell is calibrated, its compliance can change slightly under loading, especially when operating horizontally. Therefore we will calibrate the setup once using calibrated masses to verify the accuracy of the load cell and update its calibration factor if necessary.

At the moment of writing the signal conditioner for the load cell was not yet installed. Despite this we've performed a preliminary calibration assuming the force constant provided by the manufacturer, 0.29 N/A; We applied a ramp of from 0 to 340 mA in 20 mA steps, each step lasting for 6 seconds to allow the signal to settle sufficiently. The mean and standard deviation of the last 3 seconds of each step where calculated an plotted vs the thrust here shown in figure 8. The black line is the raw data (as a function of time) of the balance displacement (d_2) scaled to have the mean values (blue dots) centered on the corresponding step. The orange line is plotted along the right axis and corresponds to the standard deviation of the mean.

[h]

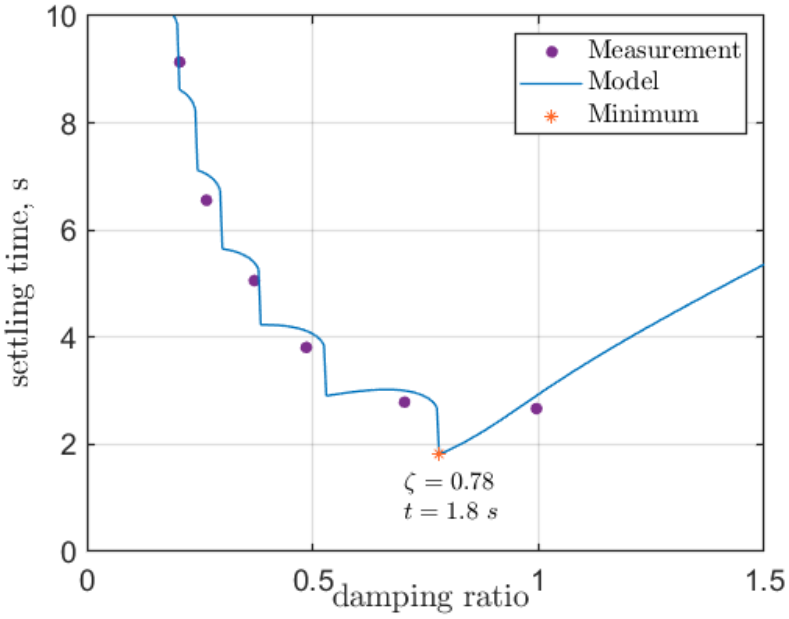

Figure 7. Settling time as a function of damping ratio.

Generally the standard deviation has a value of about 2 μm with some excursions to 5 μm due to increase ambient vibrations. Lastly the blue line is a linear fit through the mean values with equation $y = a \cdot x + b$, with $a = (915 \pm 3)10^{-4}$ and $b = (44 \pm 3) \cdot 10^{-3}$; the R^2 of the fit was equal to 1 up to the fourth decimal.

The fact that b does not equal zero attests that the balance was not perfectly equilibrated before calibrating. In practice this constant can be used to zero the measurement. The coefficient a is proportional to the compliance of the balance. However since the calibration force is applied about 365 mm from the pivot O, while the thruster force is applied at 640 mm, this needs to be scaled by a factor 1.75 resulting in a compliance of 160 μm/mN similar to what was predicted in figure 5, assuming the weight of the primary arm and cold plate equal about 2-3 kg. If the 2 μm standard deviation is taken as a measure of the noise level this would translate to a uncertainty of about 14 μN. Measuring over longer periods could reduce this number further. However proper error analysis of the whole system needs to be performed to be able to produce the true uncertainty in the measurement.

VI. Propellant supply

Most thrusters use gaseous propellant that is supplied by the propellant management system. In experimental prototypes this is usually located outside of the vacuum chamber. Therefore the thrust balance needs to accommodate one or more propellant feed lines. In this case we opted for two feed lines to be able to feed thrusters with a hollow cathode (HET,GIT). They consist of 6 mm diameter, 1 mm wall thickness PFA tubes. To mitigate their effect on the system response they have been installed parallel to the primary arm between two Swagelok connectors; one end fixed to the mounting plate and the other end on the main structure such that the bending point is in line with the rotational pivot of the primary arm. This way they can be modeled as a cantilevered beam with length l with a load F applied on one end. According to Euler-Bernouilli beam theory the differential equation for the deflection $w(x)$ is then:

$$EI\frac{d^4w}{dx^4} = 0, \qquad w|_{x=0} = 0, \qquad \left.\frac{dw}{dx}\right|_{x=0} = 0, \qquad \left.\frac{d^2w}{dx^2}\right|_{x=l} = 0, \qquad -EI\left.\frac{d^3w}{dx^3}\right|_{x=0} = F \tag{33}$$

Where E is the Young's modulus of the material and I the second moment of area. The deflection at the end being:

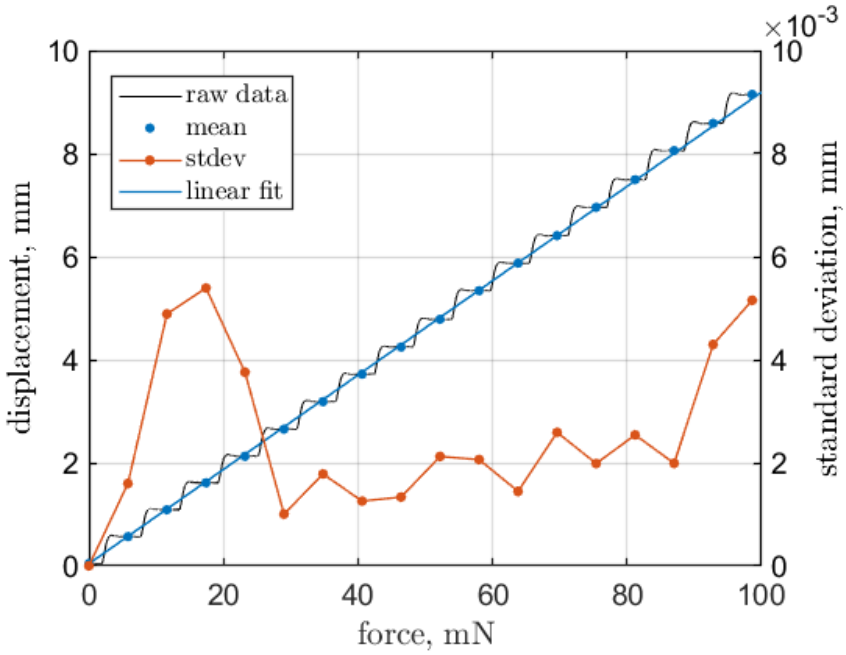

Figure 8. Preliminary calibration in the range of 0-100 mN.

$$w(l) = \frac{Fl^3}{3EJ} \tag{34}$$

Since the angle of deflection, for small angles is $\theta \approx w/l$ and the torque is $\tau = Fl$ the corresponding rotational stiffness is $\kappa = 3EI/l$. With $l = 0.48$ m, $E = 0.6$ GPa and $I = 5.1 \cdot 10^{-11}$ m^4 this results in a stiffness of 0.2 N-m/rad per feed line, for a total stiffness of 0.40 N-m/rad, about twice the value of the pivots at O. Even on an unloaded system with a stiffness of 48.2 N-m/rad the feed lines would contribute less than 1%.

VII. Power supply

As with the propellant management system the power supply is generally separated from the thruster in an experimental setting; therefore power supply lines are needed. We opted for 4 supply lines which could power up to 2 electromagnets or the anode, keeper and the heater (2) of a HET. The electromagnet on the HPT05M consumes up to 30 A requiring at least gauge 10 wires (2.6 mm ⌀) according to MIL-STD-975. We settled for 3 mm ⌀ enamelled copper cables that can handle temperatures up to 200°C.

A. Liquid connectors

Especially for high power, power lines have a considerable diameter and introduce an excessive amounts of stiffness to the system. To mechanically decouple the power lines from from the system we included liquid metal connectors. These consist of a metal receptacle filled with a liquid metal and metal rod partially submerged in the metal liquid. Since the viscous drag on the is negligible the rod and receptacle can move freely with respect each other, all the while the electrical contact is maintained by the liquid metal.

In the past mercury was used for this purpose but this is undesirable because of it's high toxicity. Instead we used Galinstan, an eutectic mixture of gallium, indium and tin. It is liquid at room temperature $T_{fus} = -19$°C, has an electrical conductivity of $3.46 \cdot 10^6$ S/m and a vapour pressure of less than 10^{-8} mbar at 500 °C meaning it is suitable for testing in high vacuum. The problem with Galinstan is that it embrittles aluminium and other metals. Certain stainless steels (SS) and refractory metals have good resistance against embrittlement.

To accommodate the high currents we chose Molybdenum for its relatively high conductivity $1.87{\cdot}10^7$ S/m, more than 10 times that of SS. The receptacle is 15 mm diameter 23 mm long cylinder with a 12 mm diameter, 12 mm deep cylindrical cavity.

We simulated the resistive dissipation in the liquid to see whether any notable heating would occur. Figure 9 shows a radial section of liquid metal, the contour plot show the resistive dissipation while the the current density streamlines are printed in white. The total dissipation in the liquid amounts to only 12 mW while the dissipation in the receptacle is little over 14 mW and that in the rod 175 mW.

This is much less than the dissipation in the copper cables which is of the order of several Watts. However during testing of the liquid connectors a considerable temperature increase was measured, in hindsight due to an oxidized steel bolt that was used in the connection to the receptacle, instead of a more conductive metal. Based on those tests it was decided to run the cooling lines through the liquid connectors.

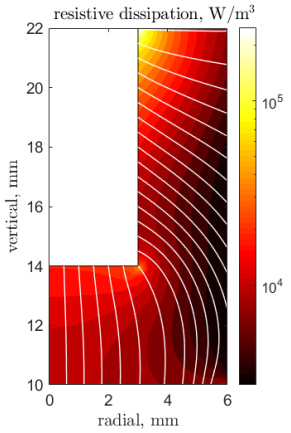

Figure 9. Resistive dissipation inside the liquid metal for a 50 A current.

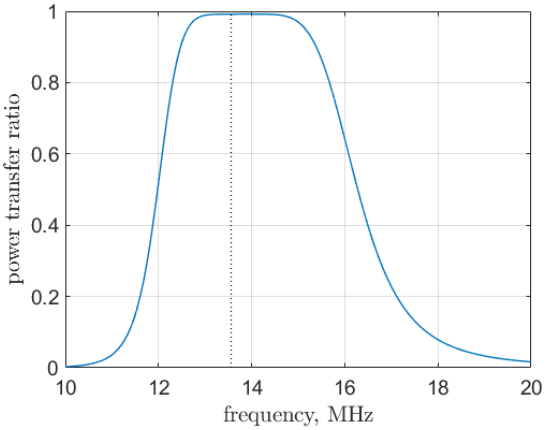

Figure 10. Ratio of power dissipated in the load to total RF power as a function of frequency.

B. Wireless power transfer

The HPT05M is powered by a 1 kW RF generator that operating at 13.56 MHz. This power is supplied to the antenna through a 10.4 mm diameter RG214 cable. The rigidity of the cable would negate the compliance of the balance. In the current prototype the antenna could be entirely decoupled from the rest of the thruster mitigating this problem. However in the next iteration the antenna and matching circuit will be integrated into the engineering model. To mechanically decouple the cable from the system we propose a wireless power transfer mechanism inspired by the current trends in wireless power transfer.

Wireless power transfer (WPT) can be achieved by two adjacent resonant RLC circuits coupled by their mutual inductance M, where the resonance frequency is given by $\omega_0 = (LC)^{-1/2}$. The equivalent circuit of the RF generator, the WPT mechanism and the thruster is shown in figure 11. Where Z_S and Z_L are the source and load (thruster) impedance.

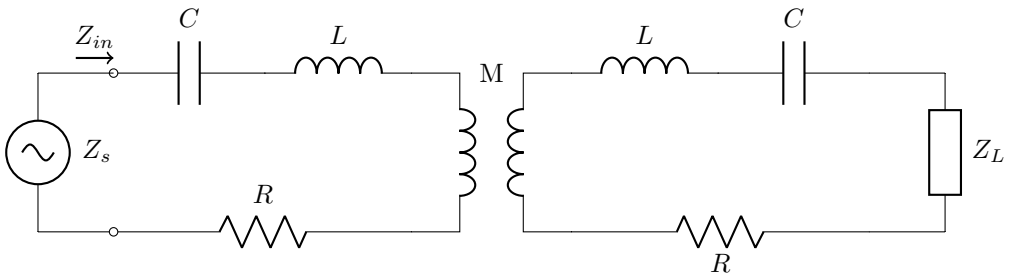

Figure 11. Circuit of a wireless power transfer mechanism.

To have efficient power transfer the impedance of system including the WPT mechanism should be

matched to that of the source impedance, i.e. $Z_s = Z_{in}$. The input impedance Z_{in} as seen by the source can be written as:

$$Z_{in} = \frac{(R + j\omega L + \frac{1}{j\omega C})(Z_L + R + j\omega L + \frac{1}{j\omega C}) + \omega^2 M^2}{Z_L + R + j\omega L + \frac{1}{j\omega C}} \tag{35}$$

When the RF generator operates at the resonance frequency, i.e $\omega = \omega_0$ the imaginary part of the input impedance goes to zero.

$$Z_{in} = R + \frac{\omega_0^2 M^2}{Z_L + R} \tag{36}$$

The thruster has an on-board matching circuit that is designed to keep the thruster impedance equal to the source impedance, so generally: $Z_L = Z_s = 50\Omega$. Equation 36 can then be solved for the mutual inductance M required for matched conditions. Generally the parasitic resistance R of the RLC circuit is much smaller than 50Ω and therefore $M \approx 0.587\mu$H. In practice the mutual inductance can be tuned by varying the distance between the two inductive coils relaxing the design tolerances.

$$M = \frac{\sqrt{Z_S^2 - R^2}}{\omega_0} \approx \frac{Z_s}{\omega_0} \tag{37}$$

The average power dissipated in the load is:

$$\langle P \rangle_L = \frac{1}{2} \mathrm{Re}\left\{V_L I_L^*\right\} \tag{38}$$

The current and voltage in the load are proportional to those in the source by some coefficient (q_V, q_I) that is a function of ω.

$$V_L = \frac{1}{1 + \frac{Z_1(j\omega M + Z_1 + Z_L)}{j\omega M(Z_1 + Z_L)}} \frac{Z_L}{Z_1 + Z_L} V_S = Q_V V_s \tag{39}$$

$$I_L = \frac{j\omega M}{Z_1 + j\omega M} I_S = Q_I I_S \tag{40}$$

$$Z_1 = \frac{1}{j\omega C} + j\omega(L - M) + R \tag{41}$$

The power transfer ratio is then simply the real part of the complex product of the two coefficients $\Gamma = \mathrm{Re}\left\{Q_V Q_I^*\right\}$, which is plotted in figure 10. The transfer ratio is around 99% for more than 1 MHz of bandwidth around the operating frequency of 13.56 MHz. Under matched conditions and an RF power of 450W the currents in the capacitors are around 4 A, with differential voltages up to 700V which is feasible for ceramic RF capacitors. The design currently exists on paper but will be implemented en tested later this year.

VIII. Electronics

To avoid a plethora of vacuum feed-through connections, the electronics of the thrust balance are mounted on the structure itself and therefore exposed to the vacuum environment. Care is to taken to avoid the use of electrolytic capacitors which can lose their electrolyte over time due to evaporation. To prevent overheating the PCB is mounted on a water cooled cold plate. An aluminium cover is placed over the electronics to prevent electromagnetic interference (EMI) due to the strong RF fields.

The electronics are based on two Arduino micro-controllers and are divided over two PCBs, the main board containing the master Arduino Due and a secondary board with the slave Arduino Nano. The secondary board is mounted on top of the thruster mounting plate (which is also cooled) and further contains an accelerometer (ADXL355), 8 PT1000 resistance temperature detector (RTD) signal conditioners and a variable current source, to power the voice coil. The main board also contains an accelerometer and 8 PT1000 signal conditioners as well as a dual axis inclinometer (ADIS16209), 3 stepper motor controllers and a signal conditioner for the load cell. There is another inclinometer on a separate small PCB that will be mounted on the secondary arm for enhanced precision. Master en slave are connected by 6 wires using the

SPI protocol. The master Arduino is connected to a PC by four wires RS485 to USB adaptor which is the only electronic connection to the ambient environment.

The inclinometers and stepper motor controllers allow for automatic leveling of the base plate. The accelerometers allow for measuring ambient vibrations which can be used to enhance the post-processing. The RTDs are used to track thermal drifts of various parts of the thrust balance. The electronic components have been defined and the PCB is currently being designed.

IX. Cooling

The HPT05M prototype operates in the 0.3-1 kW range with an efficiency of around 10%. Its electromagnets have a resistance of about 0.8Ω resulting in an Ohmic heating power of 720W at 30 A, increasing with time due to the increasing resistance with temperature. The thermal loads to the balance are therefore of the order of 1-2 kW; the need for a cooling system is obvious.

To realise this three separate water cooled cold-plates are installed: one doubling as the thruster mounting plate, a second cold plate on the main structure to cool the electronics and a smaller one passing by the liquid connectors. All three cold-plates are connected in series by means of 8 mm ⌀ SS and PFA tubing. For a total cooling line length of about 10 m and a differential pressure of 3.5 bar we estimate a flow rate of 7 L/min and Reynolds number of $1.8{\cdot}10^4$ implying turbulent flow. The thermal resistance of the mounting cold plate is about 11 °C/kW, that of the electronics plate 10 °C/kW and for the liquid connector cooling 0.06 °C/W providing sufficient cooling. What remains an open question is whether the turbulent flow will introduce vibrations that will perturb the measurement significantly; this is yet to be tested.

As with the gas lines the rigidity of the cooling lines would add stiffness to the balance. To mitigate this the connection from the fixed base to the mounting plate is done via 0.52 m semi-circular loops in a transversal plane perpendicular to the direction of displacement. Using the Autodesk Inventor's stress analysis module we estimate the total stiffness per loop to be around 1.2 N/m which translates to a rotational stiffness (of both loops) of 0.65 N-m/rad. Which is relatively large compared to the main pivots but small compared to the total stiffness of the system.

X. Conclusion

In this paper we detailed the development of a new thrust balance that was designed with the HPT05M helicon plasma thruster prototype in mind. A dynamic analysis using Lagrangian mechanics was presented adding to the kinematic analysis of Ref.[7] and it was shown that the (unloaded) system indeed behaves as a damped harmonic oscillator with an effective stiffness and moment of inertia of 12.2 kg-m^2 and 48.2 N-m/rad respectively and a natural frequency of 316 mHz. It was also shown that the stiffness of the smaller pivots actually dominates over that of the larger pivots due to the large magnification factor of 31.

An analysis of the variable damping system was also presented. It was shown that the system provided sufficient viscous damping up to critical damping and it was found that a damping ratio of 0.78 produced the shortest settling time of about 1.8 s. A notably large discrepancy between the predicted and measured damping ratios has yet to be explained.

A preliminary calibration showed a linear behaviour with a compliance of 160 μm/mN as predicted beforehand. This would mean about a 100 μm/mN compliance for with a 5 kg thruster mounted. Noise due to ambient vibrations seems to be of the order of 2-5 μ or 20-50 μN.

An analysis of both the gas lines and water cooling lines showed a negligible effect on the balance stiffness. The cooling system can dissipate about 2 kW for a temperature differential between the cooling liquid and the thruster plate of about 22 °C.

The high current power lines are mechanically decoupled using liquid metal connectors which were shown to dissipate less than 200 mW at 50 A.

Lastly a wireless power transfer mechanism was proposed that allows for mechanically decoupling the rigid high power RF cables. Such a system based on magnetic resonance coupling promises highly efficient ($> 95\%$) power transfer in a relatively wide band (1 MHz) around the operating frequency of 13.56 MHz.

Future work is centred on integrating the on-board electronics, verifying the calibration using calibration masses and a thorough error analysis of the complete system.

References

[1]Ahedo, E. and Merino, M., "Two-dimensional supersonic plasma acceleration in a magnetic nozzle," *Physics of Plasmas*, Vol. 17, No. 7, 2010, pp. 073501.

[2]Ahedo, E. and Navarro-Cavallé, J., "Helicon thruster plasma modeling: Two-dimensional fluid-dynamics and propulsive performances," *Physics of Plasmas*, Vol. 20, No. 4, 2013, pp. 043512.

[3]Tian, B., Merino, M., and Ahedo, E., "Two-dimensional plasma-wave interaction in an helicon plasma thruster with magnetic nozzle," *Plasma Sources Science and Technology*, Vol. 27, No. 11, 2018, pp. 114003.

[4]Zhou, J., Domínguez-Vázquez, A., Pérez-Grande, D., Fajardo, P., and Ahedo, E., "An axisymmetric hybrid model for the plasma transport in a helicon plasma thruster," *Space Propulsion Conference 2018*, No. 00308, Association Aéronautique et Astronautique de France, Seville, Spain, 2018.

[5]Navarro-Cavallé, J., Wijnen, M., Fajardo, P., and Ahedo, E., "Experimental characterization of a 1 kW helicon plasma thruster," *Vacuum*, Vol. 149, 2018, pp. 69–73.

[6]Navarro-Cavallé, J., Wijnen, M., Fajardo, P., Ahedo, E., Gómez, V., Giménez, A., and Ruiz, M., "Development and Characterization of the Helicon Plasma Thruster Prototype HPT-03," 36^{th} *International Electric Propulsion Conference*, No. IEPC-2019-A596, Electric Rocket Propulsion Society, Vienna, Austria, 2019.

[7]Polzin, K. A., Markusic, T. E., Stanojev, B. J., DeHoyos, A., and Spaun, B., "Thrust stand for electric propulsion performance evaluation," *Review of Scientific Instruments*, Vol. 77, No. 10, 2006, pp. 105108.

[8]Pancotti, A., Haag, T., King, S., and Walker, M., "Recommended Practices in Thrust Measurements," *33rd International Electric Propulsion Conference*, IEPC-2013-440, 2013.

[9]Bae, J.-S., Kwak, M. K., and Inman, D. J., "Vibration suppression of a cantilever beam using eddy current damper," *Journal of Sound and Vibration*, Vol. 284, No. 3-5, 2005, pp. 805–824.